

Decoupling the complex amplitudes of partial waves in two-photon ionization

Yi-Jia Mao ¹, Zhao-Han Zhang,¹ Tao Chen ¹, Hong-Bin Yao ^{2,*}, Yang Li ^{1,†} and Feng He^{1,3}

¹Key Laboratory for Laser Plasmas (Ministry of Education) and School of Physics and Astronomy, Collaborative Innovation Center for IFSA (CICIFSA), Shanghai Jiao Tong University, Shanghai 200240, China

²Key Laboratory of New Energy and Materials Research of Xinjiang Education Department, Xinjiang Institute of Engineering, Urumqi 830091, China

³CAS Center for Excellence in Ultra-Intense Laser Science, Shanghai 201800, China



(Received 27 February 2024; revised 1 May 2024; accepted 3 June 2024; published 24 June 2024)

Taking the two-photon ionization process in hydrogen atoms as an example, we propose a scheme to decouple the partial-wave information in ultrafast ionization. By analyzing the interference in the photoelectron angular distributions obtained from the solution of the time-dependent Schrödinger equation, the phase difference and amplitude ratio for different partial waves can be extracted. In the perturbative regime, the one-photon ionization by the 2ω pulse is taken as a reference to distinguish the contributions from the s and d waves in two-photon ionization. In the nonresonant cases, the phases of different partial waves in two-photon ionization are essentially the Coulomb phase shifts, which are independent of the pulse width. In the resonant case, an additional phase is accumulated during the resonant transition. The resulting time delays for both partial waves are proportional to the pulse duration. When the above-threshold ionization occurs, the continuum-continuum transition introduces an additional phase. The amplitudes of both partial waves are strongly related to the photon energy. They can be used to reveal hidden structures, such as the nonlinear Cooper minimum of different partial waves. This method of decoupling the partial-wave information can be extended to more complex atoms with photons across a wide range of energy.

DOI: [10.1103/PhysRevA.109.063117](https://doi.org/10.1103/PhysRevA.109.063117)

I. INTRODUCTION

As a fundamental process, photoionization has been widely studied since the discovery of the photoelectric effect [1]. Benefiting from the advancement of laser technologies, the observation of photoionization in experiments has been extended from single-photon processes to multiphoton regimes [2–4]. Unlike one-photon ionization, which loses its intuitiveness when the multielectron effect is involved [5–7], multiphoton ionization is already complicated due to the influence of intermediate states or continuum-continuum (CC) transitions in above-threshold ionization (ATI) [8–13]. Two-photon ionization (TPI) is the most basic case of multiphoton ionization. Understanding the amplitudes and phases of different partial waves is crucial for comprehending this dynamic process [14,15].

Photoionization is not instantaneous [16,17]. Similar to quantum scattering, the electron wave packet accumulates a phase during the ionization process, a phenomenon known as half-scattering. The partial derivative of this phase with respect to the photoelectron energy is called the Eisenbud-Wigner-Smith (EWS) delay [18–21], which represents the time it takes for an electron to absorb a photon and become ionized. The techniques of the reconstruction of attosecond beating by interference of two-photon transitions (RABBITT)

[22–26] and the attosecond streak camera (ASC) [27–32] were initially developed to characterize the attosecond pulse generated. They are now commonly used to study phase information and time delays in ionization processes.

In RABBITT studies, an attosecond pulse train (APT) with extreme ultraviolet (XUV) wavelengths and a weak near-infrared (NIR) field are utilized. While in the ASC, the APT is replaced by an isolated attosecond pulse. In both techniques, the delay between the XUV and the NIR pulses is tuned to extract the time delay in photoionization processes. The time delay consists of two parts: the EWS delay and the CC delay. The first arises from the absorption of the XUV photon, while the second provides insight into the transition process between the continuum states induced by the NIR field [17,33,34]. The CC delay is typically estimated using the Coulomb states of hydrogen-like atoms [11,15,35]. By subtracting this part from the time delay, the EWS delay can be obtained. In RABBITT experiments, the TPI processes studied contain one XUV photon and one NIR photon. As for the ASC, it can provide phase information when the electron is ionized by either one or two XUV photons.

Both techniques can be further applied to study the phase accumulated in resonant transitions [36,37]. For instance, the phase shift and the photoelectron angular distribution (PAD) of TPI via an intermediate resonant state has been studied both experimentally and theoretically with the RABBITT technique [38–40]. By employing the ASC, the time delay of two-photon resonant ionization has been extracted by Su *et al.* [41]. The delay is proportional to the applied XUV pulse

*Contact author: hbyao@mail.sdu.edu.cn

†Contact author: liyang22@sjtu.edu.cn

width. In the methodologies introduced above, the partial-wave information in TPI processes is usually not disentangled. It was reported that the time delay difference of the outgoing s and d electrons from the TPI of helium is extracted in a RABBITT experiment [42]. Recently, another theoretical work presented a method to obtain the relative phases and magnitude ratios in TPI processes for both s - and p -electron targets also by the RABBITT technique [43]. However, the contributions from different partial waves are still unable to be separated.

By applying the $\omega - 2\omega$ pulse pair technique, the information of different partial waves can be easily distinguished in TPI processes. With the assistance of the seeded free-electron laser, an $\omega - 2\omega$ pulse pair with a controlled relative phase can be generated [44]. When the pulse pair is applied to an atom, different partial wave contributions will interfere with each other in the PAD. By analyzing the PADs as a function of relative phases, the phase and amplitude information can be obtained [45–48]. Most studies only extracted the phase difference or amplitude ratio of different partial waves by this method. Nevertheless, if one primarily focuses on the scenario where the ground state is not strongly modulated, the phase and amplitude of the one-photon ionization can serve as a reference. This allows for the calculation of the phase, amplitude, and time delay of the individual partial-wave contribution in TPI. The phase accumulated in one-photon ionization of the hydrogen atom can be analytically determined by the Coulomb phase shift [49]. For other atoms, this phase can be calculated using the many-body perturbation theory or determined through experiments using the RABBITT technique [5,14].

In this study, we apply $\omega - 2\omega$ pulse pairs to distinguish the contributions from multiple partial waves in TPI. We solve the time-dependent Schrödinger equation (TDSE) to obtain the PADs resulting from pulse pairs with different relative phases in hydrogen atoms. Through the analysis of the PADs, the partial-wave phase difference and amplitude ratio can be extracted. By taking the partial-wave phase and amplitude in one-photon ionization as a reference, we are able to distinguish the contributions of the s and d waves in phases, amplitudes, and time delays. The method is applied to the cases of two-photon nonresonant, resonant, and above-threshold ionization processes. The validity of the results is confirmed and analyzed with the second-order perturbation theory and full analytical calculations in the ionization of hydrogen atoms.

This paper is organized as follows. Section II contains the details of the TDSE simulation and the decoupling of partial-wave information from the PADs. In Sec. III, the partial-wave phases and amplitudes are extracted and analyzed for two-photon nonresonant, resonant, and above-threshold ionization, respectively. Section IV provides a summary of the paper. Atomic units are applied throughout the paper unless stated otherwise.

II. NUMERICAL METHODS

A. TDSE simulations

The TDSE is numerically solved to investigate the ionization processes of the hydrogen atom by the publicly available

QPC-TDSE program developed by Zhang *et al.* [50]. The solution of the TDSE, $i\frac{\partial\psi}{\partial t} = \hat{H}\psi$, is conducted in velocity gauge, where the Hamiltonian is expressed as

$$\hat{H} = -\frac{1}{2}\nabla^2 - i\mathbf{A}(t) \cdot \nabla + V(r), \quad (1)$$

where $V(r) = -1/r$. The applied vector potential can be expressed as

$$\begin{aligned} \mathbf{A}(t) = & A_\omega \exp\left[-(2\ln 2)\frac{t^2}{T^2}\right] \sin(\omega t)\mathbf{e}_z \\ & + A_{2\omega} \exp\left[-(2\ln 2)\frac{t^2}{T^2}\right] \sin(2\omega t - \phi)\mathbf{e}_z, \end{aligned} \quad (2)$$

where ω represents the fundamental angular frequency, A_ω and $A_{2\omega}$ denote the amplitudes of the fundamental wavelength and its second harmonic, and ϕ is the relative phase between the two components. The field has a Gaussian envelope with T representing its full width at half maximum (FWHM). The tails of the Gaussian envelope are smoothly truncated to avoid any nonphysical effect in the calculation.

The TDSE is solved by expanding the wave function through 6000 eighth-order B-spline functions, denoted as $B_n(r)$, defined on a knot sequence that is linearly spaced in the radial direction, and 12 spherical harmonics, labeled as $Y_{l0}(\theta)$. The magnetic quantum number of the spherical harmonics can be set to zero, as the applied fields are all linearly polarized.

We diagonalize the Hamiltonian to calculate the ground-state wave function and propagate the wave function by the Crank-Nicolson method with a step size of $\Delta t = 0.008$ a.u. The simulations are conducted in a spherical box with a maximum radius of $R_{\max} = 2500$ a.u. and an absorbing boundary lies at $R_a = 2450$ a.u. When the wave function propagates to the boundary, it is smoothly absorbed by the mask function $\cos^\alpha[\pi(r - R_a)/2(R_{\max} - R_a)]$, where $\alpha = 0.002$. At the end of the propagation, the final wave function is projected onto the field-free Coulomb continuum states with incoming boundary conditions to obtain the angle-resolved photoelectron momentum distribution (PMD) [51–53]. The projection first evaluates the partial wave PMDs with different angular quantum numbers, which are denoted as $M_{l0}(k)$. For the photoelectron with energy E , where $E = k^2/2$, its Coulomb phase shift is [49]

$$\Delta_l(E) = \arg\left[\Gamma\left(l + 1 - \frac{i}{\sqrt{2E}}\right)\right]. \quad (3)$$

Then the angle-resolved PMD is calculated as

$$I(k, \theta) = \left| \sum_l (-i)^l e^{i\Delta_l(k^2/2)} Y_{l0}(\theta) M_{l0}(k) \right|^2. \quad (4)$$

B. Decoupling of partial-wave information through photoelectron angular distributions

We take the electron initially located in the s orbital as an example. The extension of this method to the p_0 electron can be found in Appendix A. When an $\omega - 2\omega$ pulse pair acts on the electron, it can be ionized to the same continuum state by absorbing either one 2ω photon or two ω photons. The first process leads to the p wave, while the second results

in the s and d waves. The amplitudes of the three partial wave terms are denoted as c_s , c_p , and c_d . Their corresponding phases, which exclude the centrifugal-potential phase, $-l\pi/2$, are written as σ_s , σ_p , and σ_d . The PAD at energy E can be calculated as

$$I(E, \theta) = |c_s(E)e^{i\sigma_{sd}(E)}Y_{00}(\theta) + c_p(E)e^{i\sigma_{pd}(E)+i(\phi-\pi/2)}Y_{10}(\theta) - c_d(E)Y_{20}(\theta)|^2, \quad (5)$$

where $\sigma_{sd} = \sigma_s - \sigma_d$ and $\sigma_{pd} = \sigma_p - \sigma_d$. Since $Y_{l0}(\theta) = \sqrt{\frac{2l+1}{4\pi}}P_l(\cos\theta)$ and the maximum l in Eq. (5) is 2, $I(E, \theta)$ can be also expanded as

$$I(E, \theta) \propto 1 + \sum_{k=1}^4 \beta_k(E)P_k(\cos\theta), \quad (6)$$

where $P_k(\cos\theta)$ is the Legendre polynomial of order k and β_k is the corresponding coefficient. From Eq. (5), we can calculate that [45,46]

$$\beta_1 = \frac{2\sqrt{3}[-2\sqrt{5}c_p c_d \sin(\sigma_{pd} + \phi) + 5c_p c_s \sin(\sigma_{ps} + \phi)]}{5(c_s^2 + c_p^2 + c_d^2)}, \quad (7a)$$

$$\beta_2 = \frac{2[5c_d^2 + 7c_p^2 - 7\sqrt{5}c_d c_s \cos(\sigma_{sd})]}{7(c_s^2 + c_p^2 + c_d^2)}, \quad (7b)$$

$$\beta_3 = -\frac{6\sqrt{15}c_p c_d \sin(\sigma_{pd} + \phi)}{5(c_s^2 + c_p^2 + c_d^2)}, \quad (7c)$$

$$\beta_4 = \frac{18c_d^2}{7(c_s^2 + c_p^2 + c_d^2)}, \quad (7d)$$

$$\beta_1 - \frac{2}{3}\beta_3 = \frac{2\sqrt{3}c_p c_s \sin(\sigma_{ps} + \phi)}{c_s^2 + c_p^2 + c_d^2}. \quad (7e)$$

In the TDSE simulation, the PADs with different ϕ are calculated. By projecting the PADs onto the Legendre polynomials, the ϕ -dependent β parameters can be obtained. Define $A = 6\sqrt{15}c_p c_d / 5(c_s^2 + c_p^2 + c_d^2)$ and $B = 2\sqrt{3}c_p c_s / (c_s^2 + c_p^2 + c_d^2)$. From Eqs. (7c) and (7e), we can fit β_3 and $\beta_1 - 2\beta_3/3$ with respect to ϕ to get σ_{ps} , σ_{pd} , A , and B . Since the one-photon ionization process, which leads to the p wave, is straightforward, it can be treated as a reference. c_p can be measured by the ionization amplitude when only a 2ω pulse is applied, while the phase is given by the Coulomb phase shift $\Delta_p(E)$. Then the phases and amplitudes for the s and d waves can be separated as

$$\sigma_s = \Delta_p - \sigma_{ps}, \quad (8a)$$

$$\sigma_d = \Delta_p - \sigma_{pd}, \quad (8b)$$

$$c_s = \frac{7\sqrt{3}Bc_p\beta_4}{5A^2}, \quad (8c)$$

$$c_d = \frac{7\sqrt{15}c_p\beta_4}{15A}. \quad (8d)$$

The time delay in TPI for different partial waves can be calculated as [19,21]

$$\tau_l = \left. \frac{\partial \sigma_l}{\partial E} \right|_{E=E_0}, \quad (9)$$

where $E_0 = 2\omega - I_p$ and I_p is the ionization energy.

III. RESULTS AND DISCUSSION

According to the selection rule [54], TPI in atoms induced by a linearly polarized field is always accompanied by two

or three different partial waves. Although these contributions show up simultaneously, their behaviors are quite different due to the intrinsic structure of the atom. Figure 1 depicts the TPI processes of hydrogen atoms studied in this work. The $1s$ electron can be ionized to s and d waves after absorbing two ω photons. The PAD of TPI is strongly correlated with the laser frequency applied. In essence, this is due to the interference between the s and d waves. By simultaneously applying the second harmonic, the resulting p wave will join the interference, leading to an asymmetric PAD. Taking this one-photon ionization pathway as a reference, the contributions from the s and d components can be decoupled by the method in Sec. II B. The phases and amplitudes of the s and d waves are then examined to discover the hidden structures in two-photon nonresonant ionization and the effect of intermediate resonant states or CC transitions.

A. Two-photon nonresonant ionization

To better assess the factors that affect the phases and amplitudes of different partial waves, we first focus on the nonresonant cases. Pulse pairs with the fundamental frequencies of $\omega = 0.35$ a.u. and $\omega = 0.4$ a.u. are applied. For the first, the laser intensities of the fundamental component I_ω and its second harmonic $I_{2\omega}$ are 2×10^{11} W/cm² and 2×10^{10} W/cm², respectively. While for the second, $I_\omega = 1 \times 10^{12}$ W/cm² and $I_{2\omega} = 2 \times 10^{10}$ W/cm². The intensities are adjusted to ensure that the ratios c_s/c_p and c_d/c_p are neither too large nor too small, which is crucial for the accuracy of the fitting from Eqs. (7c) and (7e). Under these laser intensities, the processes are still within the perturbative regime. The FWHM of the pulse pairs varies from 6 fs to 10 fs. For each

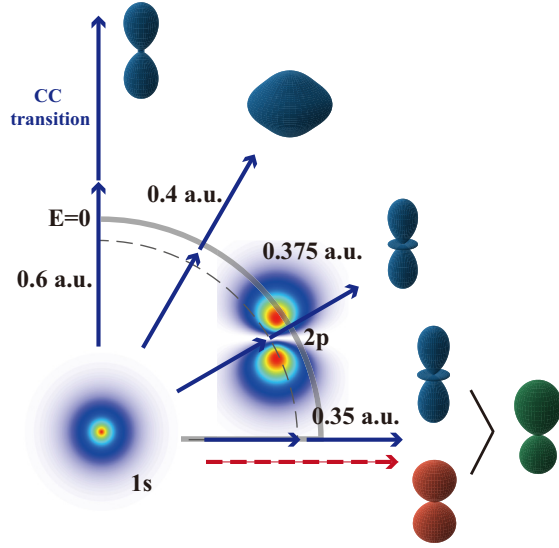


FIG. 1. The schematic diagram illustrates the TPI processes in hydrogen atoms with different laser frequencies. The blue arrows show the four cases with $\omega = 0.35, 0.375, 0.4$, and 0.6 a.u. Their respective PADs with the same color are located at the end of the arrows. The red dashed arrow demonstrates the second harmonic of $\omega = 0.35$ a.u. The resulting red PAD interferes with the blue one from the ω pulse, which leads to the PAD in green. For other frequencies studied, their corresponding second harmonics are also applied. For $\omega = 0.375$ a.u., the TPI passes through the $2p$ state. For $\omega = 0.6$ a.u., the process undergoes an extra CC transition.

laser frequency, the PADs are calculated by the TDSE simulation near their respective E_0 . The calculations are repeated for ϕ ranging from 0 to 2π . Then the β parameters derived from the PADs are fitted to obtain σ_{ps} , σ_{pd} , A , and B . From Eqs. (8a) to (8d), the separated phases or amplitudes of the s and d waves can be extracted. The values of σ_s and σ_d at E_0 for $\omega = 0.35$ a.u. and $\omega = 0.4$ a.u. are shown in Fig. 2(a). The isolated points represent the extracted values for different FWHM, while the corresponding lines show the values of the Coulomb phase shifts $\Delta_l(E)$ as calculated by Eq. (3). The extracted σ_l is independent of the FWHM and agrees well with Δ_l . This indicates that the partial-wave phases in two-photon nonresonant ionization are essentially the Coulomb phase shifts.

By taking the partial derivative of the phases with respect to the photoelectron energy at E_0 as Eq. (9), one can obtain their corresponding time delays τ_s and τ_d , as shown in Fig. 2(b). The isolated points are calculated from σ_s and σ_d , while the lines are calculated with Δ_s and Δ_d . Similar to the phases, the points and lines align closely and remain unchanged with the increase of the pulse width. This demonstrates that the time delay in TPI without passing through any intermediate state is a fixed value related to the intrinsic structure of the atom.

The spectral widths of the driven pulse pairs allow for extracting the complex amplitude of the partial waves within an energy interval near E_0 . The phase variation as a function of the photoelectron energy should follow the change of the Coulomb phase shift. This is true for the case of $\omega = 0.35$ a.u. However, when $\omega = 0.4$ a.u., an additional π phase jump

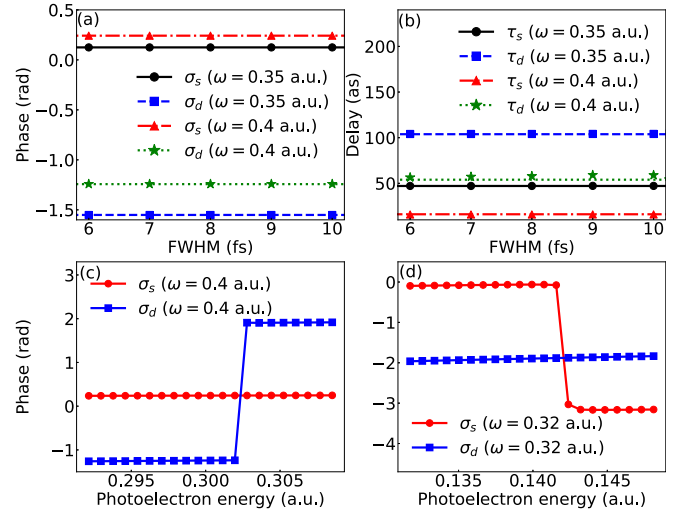


FIG. 2. (a,b) The phases and time delays for $\omega = 0.35$ a.u. and $\omega = 0.4$ a.u. at their corresponding E_0 . The isolated points are extracted values from the β parameters for T ranging from 6 fs to 10 fs. The lines correspond to the results calculated by the Coulomb phase shifts. (c) Extracted σ_s and σ_d for $\omega = 0.4$ a.u. with $T = 8$ fs in the energy domain around E_0 . (d) Same as (c) but for $\omega = 0.32$ a.u.

occurs for σ_d , while the σ_s in this case still changes smoothly as Δ_s as is shown in Fig. 2(c). From this phenomenon, one can infer that there may exist hidden structures for different partial waves in the atom. Similar to the resonance with an intermediate state, such structures are stimulated when specific photon energy is applied. To find similar structures, we gradually reduce the fundamental frequency from $\omega = 0.35$ a.u. with fixed intensities. When ω is tuned to 0.32 a.u., another π phase shift occurs. However, instead of σ_d , σ_s undergoes the phase shift in this case. The phase jump for $\omega = 0.32$ a.u. is shown in Fig. 2(d).

To elucidate the π phase jump in the energy domain, the partial-wave amplitudes are investigated. Figure 3(a) displays the results of c_s and c_d for $\omega = 0.32$ a.u. The dots and squares represent the extracted values from the β parameters for the s and d waves, respectively. While the solid and dashed curves are their counterparts directly obtained from the TDSE calculation. These two results are consistent with each other and in this case, the d wave is dominant. Both phenomena can also be observed when $\omega = 0.35$ a.u. as demonstrated by Fig. 3(b). The main distinction between the two cases lies in the number of peaks. In contrast to the single peaks of both partial waves when $\omega = 0.35$ a.u., the peak of the s wave splits into two for $\omega = 0.32$ a.u., leading to a local minimum in the middle. The energies where the local minimum exists and the phase jump occurs in Fig. 2(d) coincide with each other, indicating the possible existence of the nonlinear Cooper minimum in TPI for the s wave [55,56].

As for the case of $\omega = 0.4$ a.u., the s wave dominates the TPI. However, the extracted values of c_s and c_d match poorly with the results from the TDSE calculation, as shown in Fig. 3(c), especially when the energy approaches the π phase jump in Fig. 2(c). This manifests that the method for extracting amplitudes is not valid around the photoelectron

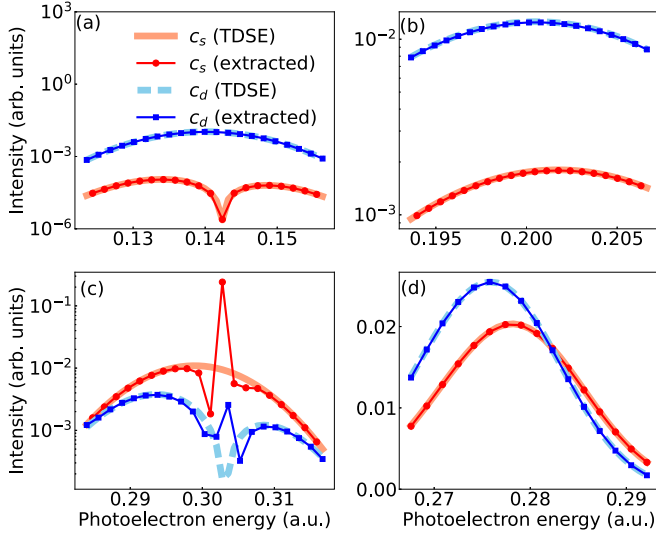


FIG. 3. (a) The amplitudes of the s and d waves as a function of the photoelectron energy for $\omega = 0.32$ a.u. with $T = 8$ fs. The isolated points are extracted from the β parameters and the bold curves are directly obtained from the TDSE calculation. (b)–(d) Same as (a) but for $\omega = 0.35, 0.4$, and 0.39 a.u.

energy where the π phase jump occurs for the d wave. From Eq. (7d) and the expression of A , one can find that when c_d is small, the values of β_4 and A will also be tiny. At this time, the accuracy of the extracted β_4 and A from the PADs is greatly affected. Since the amplitudes, c_s and c_d , retrieved by Eqs. (8c) and (8d) are sensitive to these two terms, the inaccuracy of β_4 and A will finally be transferred to the extracted c_s and c_d . Combined with the nonlinear Cooper minimum of the s wave, we can speculate that a similar local minimum may exist for the d wave near the E_0 when $\omega = 0.4$ a.u. To avoid the inaccurate extraction of the amplitudes, we attempt using $\omega = 0.39$ a.u. with the same intensities as $\omega = 0.4$ a.u. In this case, the results become consistent again, as illustrated in Fig. 3(d). Although the minimum is unable to be found with this laser frequency, it is discovered that there is a specific point in the energy domain where the dominance of the s or d wave reverses. The trend of change for the d wave is in line with the assumption that a local minimum exists at $\omega = 0.4$ a.u.

To validate our assumptions, the TPI cross section in hydrogen atoms is calculated. Figure 4 depicts the respective cross sections for the s wave, d wave, and their summation, as referenced in the work by Benda and Karule [57,58]. The photon energy in this figure can be converted to the photoelectron energy by $E_0 = 2\omega - I_p$. The trend of the ionization cross section aligns with that of c_s and c_d . One can observe that the nonlinear Cooper minimum appears for the s wave near $\omega = 0.32$ a.u. Therefore, it is clear that the d wave dominates near $\omega = 0.32$ a.u. and the splitting peak of c_s directly reflects the minimum for the s -wave ionization cross section. Near $\omega = 0.39$ a.u., the ionization cross sections of two partial waves intersect. Modulated by the spectrum of the fundamental pulse, the intersection is mapped onto the partial-wave energy spectra. Around $\omega = 0.4$ a.u., there is indeed a nonlinear Cooper minimum for the d wave, which can adequately

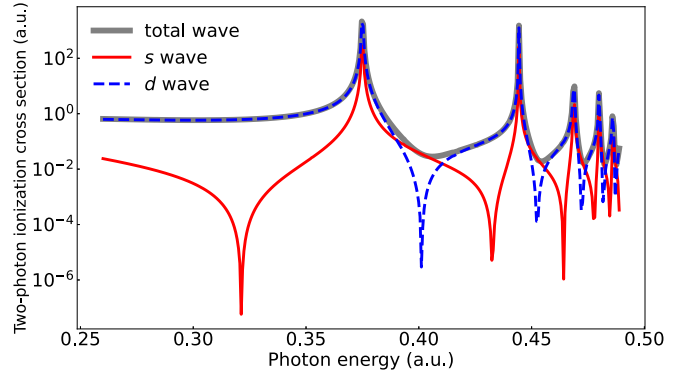


FIG. 4. Two-photon ionization cross section in hydrogen atoms for s wave, d wave, and their summation.

explain the π phase jump as well as the poor extraction of amplitudes. By comparing the extracted results and the TPI cross section, our method to unravel the concealed structures in atoms is validated. For other atoms, their ionization cross sections are usually unable to be separated analytically. The method proposed here paves the way for the experimental measurement of partial-wave-resolved hidden structures. An example of extracting the phases and amplitudes of different partial waves for the two-photon nonresonant ionization in neon is presented in Appendix B.

B. Two-photon resonant ionization

When an electron is ionized by two photons via an intermediate resonant state, the phase will be significantly altered. We apply a pulse pair with $\omega = 0.375$ a.u., the resonant frequency between the $1s$ and $2p$ states, to study two-photon resonant ionization. The laser intensities are $I_\omega = 4 \times 10^{10}$ W/cm² and $I_{2\omega} = 2 \times 10^{10}$ W/cm². The pulse width is varied in the same way as in the previous section. Figure 5(a) illustrates the phases of different partial waves in this case. The red dots represent the phases for the s wave extracted from the β parameters, while the blue squares correspond to the phases for the d wave. The bold lines show the Coulomb phase shifts. One can observe that the phases for the resonant case differ

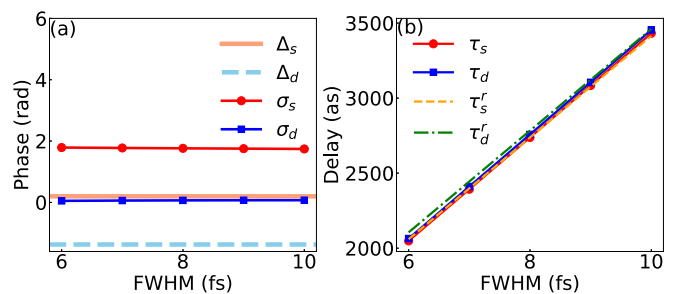


FIG. 5. (a) Extracted σ_s and σ_d from the β parameters and calculated Coulomb phase shifts Δ_s and Δ_d for $\omega = 0.375$ a.u. The data points are calculated for T from 6 fs to 10 fs. (b) The time delays τ_s and τ_d are calculated from the extracted σ_s and σ_d , respectively. The orange and green dashed lines are the results calculated by the second-order perturbation theory.

from their Coulomb phase shift counterparts. In addition, the phases change slightly as a function of T .

Since phase accumulation is closely associated with time, we can infer that the time required for TPI can be strongly modulated by an intermediate resonant state. To gain a more straightforward insight into this phenomenon, we examine the associated time delay. The time delays for the s and d waves are shown in Fig. 5(b). The delays are proportional to the pulse duration. The results presented here are consistent with the findings of Su *et al.* [41]. As a compliment to the previous study, the s and d wave contributions here can be separated. The behaviors of both partial waves look similar and their time delays are much larger than their respective EWS delays. As a result, one can infer that the additional time delay stemming from the two-photon resonant ionization is much larger than the EWS delay, which makes the difference between the two partial waves less significant.

By employing the second-order perturbation approach, we aim to replicate the phenomenon analytically. The initial state $|i\rangle$, an arbitrary intermediate state, and the final continuum state are labeled as $|i\rangle$, $|m\rangle$, and $|f\rangle$, respectively. For a laser pulse with the central frequency ω , only the final state with the expected photoelectron energy E_0 is considered, where $E_0 = 2\omega - I_p$. If the laser pulse is polarized in the z direction, the ionization amplitude c_f for the TPI process can be approximately calculated in length gauge as [10]

$$c_f = \sum_m \int_{-\infty}^{\infty} dt \left\{ \mu_{fm} e^{i\Delta E_{fm}t} f(t) \left[\int_{-\infty}^t dt' \mu_{mi} e^{i\Delta E_{mi}t'} f(t') \right] \right\}, \quad (10)$$

where $\mu_{fm} = \langle f|z|m\rangle$ and $\mu_{mi} = \langle m|z|i\rangle$ are the transition dipole moments, $\Delta E_{fm} = E_0 - E_m - \omega$, $\Delta E_{mi} = E_m + I_p - \omega$, and $f(t)$ is the pulse envelope. According to the relation between ω and E_0 , $\Delta E_{fm} = -\Delta E_{mi}$. In length gauge, the Gaussian pulse envelope applied in our scheme can be written as $f(t) = \mathcal{E}_0 \exp(-2 \ln 2 \frac{t^2}{T^2})$, where \mathcal{E}_0 is the electric field intensity. Define T_0 as $T/2\sqrt{\ln 2}$, the integral can be analytically calculated as

$$c_f = \pi \mathcal{E}_0^2 T_0^2 \sum_m \left\{ \mu_{fm} \mu_{mi} \left[e^{-(\Delta E_m T_0)^2} - i \frac{2}{\sqrt{\pi}} F(\Delta E_m T_0) \right] \right\}, \quad (11)$$

where $F(x)$ is the Dawson's integral [59].

When a resonant frequency is applied, the ionization via the resonant state within the spectral width, labeled as $|r\rangle$, will dominate the entire process. If other intermediate states are disregarded in the summation of the states, the ionization amplitude can be simplified as [41]

$$c_f = \pi \mathcal{E}_0^2 T_0^2 \mu_{fr} \mu_{ri} \left[e^{-(\Delta E_r T_0)^2} - i \frac{2}{\sqrt{\pi}} F(\Delta E_r T_0) \right]. \quad (12)$$

Since $|i\rangle$ and $|r\rangle$ are bound states, μ_{ri} is real, and the phase of $\mu_{fr} \mu_{ri}$ is essentially the Coulomb phase shift originating from the continuum state $|f\rangle$. As a result, the phases of the resonant ionization pathway for different partial waves at E_0 is

$$\sigma_f^r(E_0) = \arg[c_f(E_0)] = \Delta_f(E_0) + \theta(E_0), \quad (13)$$

where

$$\theta(E_0) = -\arctan \left[\frac{2}{\sqrt{\pi}} e^{(\Delta E_r T_0)^2} F(\Delta E_r T_0) \right]. \quad (14)$$

Since θ is a function of E_0 , from Eq. (9), the time delay from this phase term, denoted as τ^* , can be calculated by its partial derivative with respect to E_0 . Based on

$$\frac{\partial \theta}{\partial \Delta E_r} = -\frac{2e^{(\Delta E_r T_0)^2} T_0}{\sqrt{\pi} \{1 + \text{Erfi}[(\Delta E_r T_0)^2]\}}, \quad (15)$$

we can calculate that

$$\tau^* = \frac{\partial \theta}{\partial E_0} = \frac{\partial \theta}{\partial \Delta E_r} \frac{\partial \Delta E_r}{\partial E_0} = \frac{e^{(\Delta E_r T_0)^2} T_0}{\sqrt{\pi} \{1 + \text{Erfi}[(\Delta E_r T_0)^2]\}}, \quad (16)$$

where $\text{Erfi}(x)$ is the imaginary error function. As a result, the time delays for different partial waves of the resonant transition pathway can be written as

$$\tau_f^r = \frac{\partial \sigma_f^r}{\partial E_0} = \frac{\partial \Delta_f}{\partial E} \Big|_{E=E_0} + \tau^*. \quad (17)$$

For $\omega = 0.375$ a.u., the pulse is resonant with the $1s$ and $2p$ states. At this time, $\Delta E_r = 0$ and $\tau^* = T_0/\sqrt{\pi}$. The calculated τ_s^r and τ_d^r are the orange and green dashed lines in Fig. 5(b). The results from the β parameters agree well with the analytical results obtained from the perturbation approach. This proves that the time delay in two-photon resonant ionization is proportional to the pulse width applied and mainly originates from the resonant ionization pathway. In Eq. (17), only one frequency component is considered. However, for short pulses with large spectral widths, the effect of other frequency components is not negligible. Therefore, there exists a difference between τ_d and τ_d^r when T is small. In Appendix B, the analytical model developed here agrees well with the time delay in the two-photon resonant ionization in neon, indicating the universality of this analysis.

C. Two-photon above-threshold ionization

The CC delay in the RABBITT or ASC technique is typically regarded as the coupling between the NIR field and the long tail of the Coulomb potential. As for the case of two-photon ATI, the absorption of the second XUV photon in the TPI process also involves a CC transition, resulting in an additional phase shift, ϕ_{cc}^s and ϕ_{cc}^d , in the partial-wave phase. The red dots and blue squares in Fig. 6(a) show the extracted values of σ_s and σ_d , respectively, for ω ranging from 0.56 a.u. to 0.64 a.u. with $T = 8$ fs. The applied intensities are $I_{\omega} = 1 \times 10^{12}$ W/cm² and $I_{2\omega} = 2 \times 10^{10}$ W/cm². The corresponding red and blue solid curves represent the two-photon ATI phases calculated by the analytical scattering states of hydrogen atoms [60]. One can see that the two results are in good agreement with each other.

By subtracting the Coulomb phase shift at $\omega - I_p$ from the extracted partial-wave phase, we can calculate the CC phase accumulated in absorbing the second photon. The calculated and analytical results are shown in Fig. 6(b). The s and d waves accumulate different phases during the CC transition.

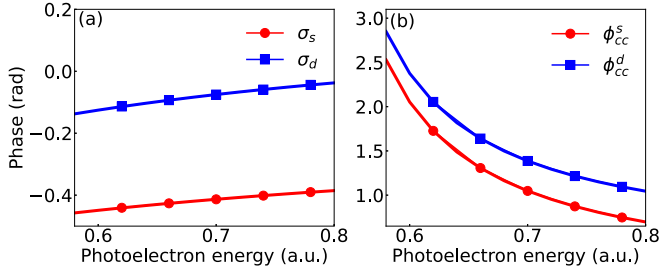


FIG. 6. (a) Extracted σ_s (red dots) and σ_d (blue squares) for ω from 0.56 a.u. to 0.64 a.u. with $T = 8$ fs. The red and blue solid curves correspond to the analytically calculated values. (b) Same as (a), but for the CC phase calculated by subtracting the Coulomb phase shift from the partial-wave phase.

Both of them decrease at a slower and slower rate as the increase of photoelectron energy.

IV. CONCLUSION

By utilizing the $\omega - 2\omega$ pulse pair, we propose a scheme to distinguish the amplitudes and phases of the s and d partial waves in TPI of hydrogen atoms. The interference of different partial waves in the PAD allows for the determination of their phase difference and amplitude ratio. By plugging in the partial-wave amplitude and phase in one-photon ionization, the mixed s and d wave contributions can be decoupled.

This method is applied to study the case where the ω pulse is nonresonant with any intermediate state, resonant with a specific state, or the ATI occurs. For the nonresonant case, the partial-wave phase is the Coulomb phase shift. Some hidden structures, like the nonlinear Cooper minimum, can be found by a sudden π phase shift in the energy domain or the extracted partial-wave amplitudes. For the resonant case, the time delays of both partial waves in two-photon resonant ionization are proportional to the pulse widths applied. When two-photon ATI occurs, the electron will accumulate an additional CC phase.

In hydrogen atoms, the partial-wave phase in one-photon ionization can be calculated by the Coulomb phase shift. For other atoms, the phase can be measured by a scheme supported by the RABBITT technique. So, this method of decoupling the complex amplitudes of partial waves can be extended to more complex atoms. In addition to the partial-wave amplitudes and phases, such interferometric schemes with bichromatic fields, $m\omega - n\omega$, can be further applied to study other effects in atoms, like the circular dichroism and the dependence of ionization rate on polarization [61,62].

ACKNOWLEDGMENTS

This work was supported by the National Natural Science Foundation of China (NSFC) (Grants No. 12274294 and No. 11925405) and the Tianshan Talent Training Program of Xinjiang (Grant No. 2023TSYCJU0009). The computations in this paper were run on the π 2.0 cluster supported by the Center for High Performance Computing at Shanghai Jiao Tong University.

APPENDIX A: DECOUPLING OF PARTIAL WAVE INFORMATION FOR p_0 ELECTRONS

For atoms like neon and argon, the outer shell electrons lie in p orbitals. After absorbing two photons, the p electron can be ionized to the p wave or f wave. With a similar $\omega - 2\omega$ pulse pair technique introduced in Sec. II B, the amplitudes and phases of the p and f partial waves can be decoupled in TPI processes. Here we consider the electrons in the p_0 orbital, which leads the ionization of p orbitals. Since only $\omega - 2\omega$ pulse pairs with linear polarization are considered, only states with $m = 0$ are considered. Therefore, the subscript 0 for different partial waves is omitted in the following discussion. Unlike the simpler s electron case, s and d waves co-occur for the p_0 electron with the absorption of one linearly polarized 2ω photon. The PAD induced by an $\omega - 2\omega$ pulse pair with relative phase ϕ at energy E is calculated as

$$I(\theta) = |c_s e^{i(\eta_s + \phi)} Y_{00}(\theta) + c_p e^{i\eta_p} Y_{10}(\theta) + c_d e^{i(\eta_d + \phi)} Y_{20}(\theta) + c_f e^{i\eta_f} Y_{30}(\theta)|^2, \quad (\text{A1})$$

where c_l and η_l ($l = s, p, d, f$ or $0, 1, 2, 3$) are the amplitudes and phases of different partial waves. The PAD can be similarly expanded as Eq. (6), but with Legendre polynomials up to order 6. The corresponding six β parameters can be calculated as

$$\beta_1 = \frac{1}{C} \left[\frac{18}{\sqrt{35}} c_d c_f \cos(\eta_{df} + \phi) + 4\sqrt{\frac{3}{5}} c_d c_p \cos(\eta_{dp} + \phi) + 2\sqrt{3} c_s c_p \cos(\eta_{sp} + \phi) \right], \quad (\text{A2})$$

$$\beta_2 = \frac{1}{C} \left[2\sqrt{5} c_d c_s \cos(\eta_{ds}) + \frac{10}{7} c_d^2 + 6\sqrt{\frac{3}{7}} c_f c_p \cos(\eta_{fp}) + \frac{4}{3} c_f^2 + 2c_p^2 \right], \quad (\text{A3})$$

$$\beta_3 = \frac{1}{C} \left[\frac{8}{3} \sqrt{\frac{7}{5}} c_d c_f \cos(\eta_{df} + \phi) + 6\sqrt{\frac{3}{5}} c_d c_p \cos(\eta_{dp} + \phi) + 2\sqrt{7} c_s c_f \cos(\eta_{sf} + \phi) \right], \quad (\text{A4})$$

$$\beta_4 = \frac{1}{C} \left[\frac{18}{7} c_d^2 + 8\sqrt{\frac{3}{7}} c_f c_p \cos(\eta_{fp}) + \frac{18}{11} c_f^2 \right], \quad (\text{A5})$$

$$\beta_5 = \frac{20}{3C} \sqrt{\frac{5}{7}} c_d c_f \cos(\eta_{df} + \phi), \quad (\text{A6})$$

$$\beta_6 = \frac{100}{33C} c_f^2, \quad (\text{A7})$$

where $C = c_s^2 + c_p^2 + c_d^2 + c_f^2$ and $\eta_{ll'} = \eta_l - \eta_{l'}$.

The six β parameters can be obtained in the same way as the s electron by projecting the calculated PAD onto the Legendre polynomials. Although the one-photon ionization for the p electron involves two different partial waves, it is possible to distinguish between them. In the TDSE simulation, where a model potential is applied, the phases for different

partial waves can be directly calculated, leading to a combination of the Coulomb phase shift, Δ_l , and phase shift induced by the short-range potential, δ_l . As for the amplitudes, they can be directly extracted separately. In experiments, both the phases and the amplitudes can be acquired through the RABBITT technique [14]. Therefore, the amplitudes and phases from the one-photon ionization can be taken as a reference and the separation of the p and f wave contributions can be realized.

c_s, c_d, η_s , and η_d are now considered as known parameters. From the fitting of β_5 with respect to ϕ, η_{df} , and $c_d c_f / C$ can be calculated. Then η_f and $\alpha_f = c_f / C$ are calculated if the d wave contribution is plugged in. Now β_3 can be reformed into $\tilde{\beta}_3$ by

$$\begin{aligned} \tilde{\beta}_3 &= \beta_3 - \frac{14}{25}\beta_5 - 2\sqrt{7}c_s\alpha_f \cos(\eta_s - \eta_f + \phi) \\ &= \frac{6}{C}\sqrt{\frac{3}{5}}c_d c_p \cos(\eta_d - \eta_p + \phi). \end{aligned} \quad (\text{A8})$$

Similarly, both η_p and $\alpha_p = c_p / C$ can be extracted with the fitting of $\tilde{\beta}_3$. The amplitudes can be calculated as

$$c_f = \frac{33\beta_6}{100\alpha_f}, \quad (\text{A9})$$

$$c_p = \frac{33\beta_6\alpha_p}{100\alpha_f^2}. \quad (\text{A10})$$

The η_l extracted can be connected with the phases excluding the centrifugal potential, σ_l , with

$$\sigma_l = \eta_l + \frac{l\pi}{2}. \quad (\text{A11})$$

APPENDIX B: TWO-PHOTON IONIZATION FOR p_0 ELECTRONS IN NEON

By using the TDSE simulation, we apply this scheme to study the TPI processes in neon. The Hamiltonian is in the same form as Eq. (1) but with

$$V(r) = -\frac{1 + a_1 e^{-a_2 r} + a_3 r e^{-a_4 r} + a_5 e^{-a_6 r}}{r}, \quad (\text{B1})$$

where $a_1 = 8.359, a_2 = 2.500, a_3 = -4.750, a_4 = 8.283, a_5 = 0.625$, and $a_6 = 0.640$. It is Tong-Lin's model potential for neon atoms [63,64]. The parameters of the potential are chosen from Ref. [64] for more accurate description of the excited states. By directly diagonalizing the Hamiltonian, it is calculated that the energies of the $2p$ state and $3s$ state of this model potential are -0.793 a.u. and -0.187 a.u., respectively. The $2p$ state is selected as the initial state in the following calculation. The envelope of the vector potential and the grid parameters are the same as in the case of the s electrons in hydrogen atoms, except that the number of B-spline functions is chosen as 8000. Due to the form of Tong-Lin's potential, an additional phase shift induced by the short-range potential, δ_l , is added to the Coulomb phase shift, Δ_l . The summation of these two terms can be directly obtained from the QPC-TDSE program.

For two-photon nonresonant ionization in neon, we apply $\omega = 0.681$ a.u. as the fundamental frequency. The intensities of the pulse pair are $I_\omega = 1 \times 10^{13}$ W/cm² and $I_{2\omega} = 6.3 \times 10^{10}$ W/cm². The FWHM is 8fs. By applying the method

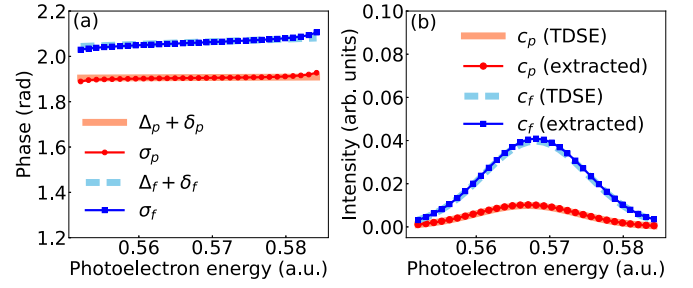


FIG. 7. (a) Extracted σ_p and σ_f from the β parameters, denoted by isolated points, in the energy domain for $\omega = 0.681$ a.u. with $T = 8$ fs in neon. The bold curves show the calculated partial-wave phase shift $\Delta_p + \delta_p$ and $\Delta_f + \delta_f$. (b) The amplitudes of the p and f waves as a function of the photoelectron energy under the same laser conditions. The isolated points are extracted from the β parameters and the bold curves are directly obtained from the TDSE calculation.

introduced in Appendix A, the amplitudes and phases of the p and f waves are decoupled. The phases are shown in Fig. 7(a), while the amplitudes are shown in Fig. 7(b). The information of the p and f waves is denoted by red dots and blue squares, respectively. The phases agree well with $\Delta_l + \delta_l$ and the amplitudes coincide with the c_p and c_f directly obtained from the TDSE calculation. Therefore, the phases of two-photon nonresonant ionization of the p_0 electron in neon are simply the summation of the Coulomb phase shift and the phase shift induced by the short-range potential. This also indicates the validity of our decoupling scheme for electrons in the p shell.

As for the two-photon resonant ionization, we choose the $3s$ state as the intermediate resonant state. The fundamental frequency of the pulse pair is selected as 0.606 a.u. The intensities are $I_\omega = 1 \times 10^{11}$ W/cm² and $I_{2\omega} = 1 \times 10^{10}$ W/cm². The FWHM ranges from 6 fs to 10 fs. Based on Eq. (9), the extracted phases for p and f waves are converted to their corresponding time delays. Both the phases and the time delays are shown in Fig. 8. It is discovered that the time delay for the p wave increases linearly with the FWHM, while the one for the f wave remains almost unchanged. We then compare the results with our model developed in Sec. III B. Equation (17) is now modified as

$$\tau_l^r = \tau_l^0 + \tau^*, \quad (\text{B2})$$

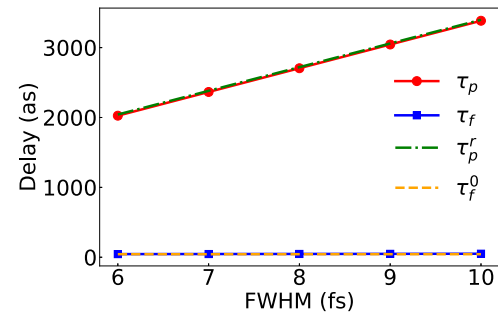


FIG. 8. The time delays for $\omega = 0.606$ a.u. τ_p and τ_f are calculated from the extracted σ_p and σ_f , respectively. The orange dashed line shows the value of τ_p^r and the green dashed line shows the result from τ_f^0 .

where

$$\tau_l^0 = \left. \frac{\partial(\Delta_l + \delta_l)}{\partial E} \right|_{E=E_0}. \quad (\text{B3})$$

We can find that τ_p^r fits well for the time delay of the p wave, while the one of the f wave aligns with τ_f^0 . This shows that the intermediate resonant state only affects the final p -wave

contribution. As for the f wave, it is still a two-photon non-resonant ionization process. This is in accordance with the fact that if the electron is ionized via the intermediate s state, the resonant ionization pathway only leads to the p wave based on the selection rule. The f wave completely originates from the nonresonant ionization pathway despite the occurrence of the resonant transition.

-
- [1] F. Krausz and M. Ivanov, *Rev. Mod. Phys.* **81**, 163 (2009).
- [2] L. A. Lompre, G. Mainfray, C. Manus, S. Repoux, and J. Thebault, *Phys. Rev. Lett.* **36**, 949 (1976).
- [3] L. A. Lompre, G. Mainfray, C. Manus, and J. Thebault, *Phys. Rev. A* **15**, 1604 (1977).
- [4] J. E. Bayfield and P. M. Koch, *Phys. Rev. Lett.* **33**, 258 (1974).
- [5] J. M. Dahlström, T. Carette, and E. Lindroth, *Phys. Rev. A* **86**, 061402(R) (2012).
- [6] D. Guénot, K. Klünder, C. L. Arnold, D. Kroon, J. M. Dahlström, M. Miranda, T. Fordell, M. Gisselbrecht, P. Johnsson, J. Mauritsson, E. Lindroth, A. Maquet, R. Täieb, A. L'Huillier, and A. S. Kheifets, *Phys. Rev. A* **85**, 053424 (2012).
- [7] L. R. Andersson and J. Burgdörfer, *Phys. Rev. Lett.* **71**, 50 (1993).
- [8] D. G. Arbó, S. D. López, and J. Burgdörfer, *Phys. Rev. A* **106**, 053101 (2022).
- [9] S. Nandi, E. Olofsson, M. Bertolino, S. Carlstrom, F. Zapata, D. Busto, C. Callegari, M. Di Fraia, P. Eng-Johnsson, R. Feifel *et al.*, *Nature (London)* **608**, 488 (2022).
- [10] K. L. Ishikawa and K. Ueda, *Phys. Rev. Lett.* **108**, 033003 (2012).
- [11] J. M. Dahlström, D. Guénot, K. Klünder, M. Gisselbrecht, J. Mauritsson, A. L'Huillier, A. Maquet, and R. Täieb, *Chem. Phys.* **414**, 53 (2013).
- [12] C. Palatchi, J. M. Dahlström, A. S. Kheifets, I. A. Ivanov, D. M. Canaday, P. Agostini, and L. F. DiMauro, *J. Phys. B* **47**, 245003 (2014).
- [13] K. Eickhoff, D. Köhnke, L. Feld, T. Bayer, and M. Wollenhaupt, *Phys. Rev. A* **105**, 053113 (2022).
- [14] J. Peschel, D. Busto, M. Plach, M. Bertolino, M. Hoflund, S. Maclot, J. Vinbladh, H. Wikmark Kreuger, F. Zapata, E. Lindroth, M. Gisselbrecht, J. Dahlström, A. L'Huillier, and P. Eng-Johnsson, *Nat. Commun.* **13**, 5205 (2022).
- [15] W. Jiang, G. S. J. Armstrong, L. Han, Y. Xu, Z. Zuo, J. Tong, P. Lu, J. M. Dahlström, K. Ueda, A. C. Brown, H. W. van der Hart, X. Gong, and J. Wu, *Phys. Rev. Lett.* **131**, 203201 (2023).
- [16] H. W. van der Hart, *Science* **328**, 1645 (2010).
- [17] J. M. Dahlström, A. L'Huillier, and A. Maquet, *J. Phys. B* **45**, 183001 (2012).
- [18] L. Eisenbud, Formal properties of nuclear collisions, Ph.D. thesis, Princeton University, 1948.
- [19] E. P. Wigner, *Phys. Rev.* **98**, 145 (1955).
- [20] F. T. Smith, *Phys. Rev.* **118**, 349 (1960).
- [21] C. de Carvalho and H. Nussenzveig, *Phys. Rep.* **364**, 83 (2002).
- [22] V. Vénier, R. Täieb, and A. Maquet, *Phys. Rev. Lett.* **74**, 4161 (1995).
- [23] P. M. Paul, E. S. Toma, P. Breger, G. Mullot, F. Augé, P. Balcou, H. G. Muller, and P. Agostini, *Science* **292**, 1689 (2001).
- [24] H. Muller, *Appl. Phys. B* **74**, s17 (2002).
- [25] K. Klünder, J. M. Dahlström, M. Gisselbrecht, T. Fordell, M. Swoboda, D. Guénot, P. Johnsson, J. Caillat, J. Mauritsson, A. Maquet, R. Täieb, and A. L'Huillier, *Phys. Rev. Lett.* **106**, 143002 (2011).
- [26] M. Han, J.-B. Ji, T. Balciunas, K. Ueda, and H. J. Wörner, *Nat. Phys.* **19**, 230 (2022).
- [27] E. Constant, V. D. Taranukhin, A. Stolow, and P. B. Corkum, *Phys. Rev. A* **56**, 3870 (1997).
- [28] E. Goulielmakis, M. Uiberacker, R. Kienberger, A. Baltuska, V. Yakovlev, A. Scrinzi, T. Westerwalbesloh, U. Kleineberg, U. Heinzmann, M. Drescher, and F. Krausz, *Science* **305**, 1267 (2004).
- [29] M. Schultze, M. Fieß, N. Karpowicz, J. Gagnon, M. Korbman, M. Hofstetter, S. Neppl, A. L. Cavalieri, Y. Komninos, T. Mercouris, C. A. Nicolaides, R. Pazourek, S. Nagele, J. Feist, J. Burgdörfer, A. M. Azzeer, R. Ernstorfer, R. Kienberger, U. Kleineberg, E. Goulielmakis *et al.*, *Science* **328**, 1658 (2010).
- [30] M. Ivanov and O. Smirnova, *Phys. Rev. Lett.* **107**, 213605 (2011).
- [31] Y. H. Kim, I. Ivanov, S. Hwang, K. Kim, C. Nam, and K. T. Kim, *Sci. Rep.* **10**, 22075 (2020).
- [32] R. Della Picca, M. F. Ciappina, M. Lewenstein, and D. G. Arbó, *Phys. Rev. A* **102**, 043106 (2020).
- [33] A. S. Kheifets, *J. Phys. B* **56**, 022001 (2023).
- [34] R. Borrego-Varillas, M. Lucchini, and M. Nisoli, *Rep. Prog. Phys.* **85**, 066401 (2022).
- [35] A. Harth, N. Douguet, K. Bartschat, R. Moshhammer, and T. Pfeifer, *Phys. Rev. A* **99**, 023410 (2019).
- [36] A. Autuori, D. Platzer, M. Lejman, G. Gallician, L. Maëder, A. Covolo, L. Bosse, M. Dalui, D. Bresteau, J.-F. Hergott, O. Tcherbakoff, H. J. B. Marroux, V. Loriot, F. Lépine, L. Poisson, R. Täieb, J. Caillat, and P. Salières, *Sci. Adv.* **8**, eabl7594 (2022).
- [37] Y. Liao, Y. Zhou, L.-W. Pi, J. Liang, Q. Ke, Y. Zhao, M. Li, and P. Lu, *Phys. Rev. A* **105**, 063110 (2022).
- [38] M. Swoboda, T. Fordell, K. Klünder, J. M. Dahlström, M. Miranda, C. Buth, K. J. Schafer, J. Mauritsson, A. L'Huillier, and M. Gisselbrecht, *Phys. Rev. Lett.* **104**, 103003 (2010).
- [39] D. M. Villeneuve, P. Hockett, M. J. J. Vrakking, and H. Niikura, *Science* **356**, 1150 (2017).
- [40] A. S. Kheifets and A. W. Bray, *Phys. Rev. A* **103**, L011101 (2021).
- [41] J. Su, H. Ni, A. Jaroń-Becker, and A. Becker, *Phys. Rev. Lett.* **113**, 263002 (2014).
- [42] J. Fuchs, N. Douguet, S. Donsa, F. Martin, J. Burgdörfer, L. Argenti, L. Cattaneo, and U. Keller, *Optica* **7**, 154 (2020).
- [43] A. S. Kheifets, *Phys. Rev. Res.* **6**, L012002 (2024).
- [44] K. C. Prince, E. Allaria, C. Callegari, R. Cucini, G. De Ninno, S. Di Mitri, B. Diviacco, E. Ferrari, P. Finetti, D. Gauthier,

- L. Giannessi, N. Mahne, G. Penco, O. Plekan, L. Raimondi, P. Rebernik, E. Roussel, C. Svetina, M. Trovò, M. Zangrando *et al.*, *Nat. Photonics* **10**, 176 (2016).
- [45] M. Di Fraia, O. Plekan, C. Callegari, K. C. Prince, L. Giannessi, E. Allaria, L. Badano, G. De Ninno, M. Trovò, B. Diviacco, D. Gauthier, N. Mirian, G. Penco, P. C. V. R. Ribič, S. Spampinati, C. Spezzani, G. Gaio, Y. Orimo, O. Tugs, T. Sato *et al.*, *Phys. Rev. Lett.* **123**, 213904 (2019).
- [46] D. You, K. Ueda, E. V. Gryzlova, A. N. Grum-Grzhimailo, M. M. Popova, E. I. Staroselskaya, O. Tugs, Y. Orimo, T. Sato, K. L. Ishikawa, P. A. Carpeggiani, T. Csizmadia, M. Füle, G. Sansone, P. K. Maraju, A. D'Elia, T. Mazza, M. Meyer, C. Callegari, M. Di Fraia *et al.*, *Phys. Rev. X* **10**, 031070 (2020).
- [47] L. Giannessi, E. Allaria, K. C. Prince, C. Callegari, G. Sansone, K. Ueda, T. Morishita, C. N. Liu, A. N. Grum-Grzhimailo, E. V. Gryzlova, N. Douguet, and K. Bartschat, *Sci. Rep.* **8**, 7774 (2018).
- [48] Y.-J. Mao, H.-B. Yao, M. He, Z.-H. Zhang, Y. Li, and F. He, *Phys. Rev. A* **108**, 053117 (2023).
- [49] K. L. Ishikawa and K. Ueda, *Appl. Sci.* **3**, 189 (2013).
- [50] Z.-H. Zhang, Y. Li, Y.-J. Mao, and F. He, *Comput. Phys. Commun.* **290**, 108787 (2023).
- [51] L. B. Madsen, L. A. A. Nikolopoulos, T. K. Kjeldsen, and J. Fernández, *Phys. Rev. A* **76**, 063407 (2007).
- [52] B. Fetić, M. Tunja, W. Becker, and D. B. Milošević, *Phys. Rev. A* **105**, 053121 (2022).
- [53] B. Fetić, W. Becker, and D. B. Milošević, *Phys. Rev. A* **102**, 023101 (2020).
- [54] C. Eckart, *Rev. Mod. Phys.* **2**, 305 (1930).
- [55] J. W. Cooper, *Phys. Rev.* **128**, 681 (1962).
- [56] J. Hofbrucker, A. V. Volotka, and S. Fritzsche, *Sci. Rep.* **10**, 3617 (2020).
- [57] J. Benda and Z. Masin, *Sci. Rep.* **11**, 11686 (2021).
- [58] E. Karule, *J. Phys. B* **11**, 441 (1978).
- [59] F. W. J. Olver, D. W. Lozier, R. F. Boisvert, and C. W. Clark, *NIST Handbook of Mathematical Functions* (Cambridge University Press, New York, NY, 2010).
- [60] A. P. Jayadevan and R. B. Thayyullathil, *J. Phys. B* **34**, 699 (2001).
- [61] A. V. Volotka, J. Hofbrucker, and S. Fritzsche, *Phys. Rev. A* **104**, L031103 (2021).
- [62] J. Hofbrucker, S. Ramakrishna, A. V. Volotka, and S. Fritzsche, *Phys. Rev. A* **106**, 013118 (2022).
- [63] X. M. Tong and C. D. Lin, *J. Phys. B* **38**, 2593 (2005).
- [64] S.-F. Zhao, N. Wang, Y.-J. Li, Z. Guan, G.-L. Wang, T. Morishita, and P.-C. Li, *J. Phys. B* **54**, 175601 (2021).